JGR Planets

Key Points:

- Salty oceans near the freezing point develop buoyant plumes which rise in the water column when energized by localized hydrothermal vents
- Buoyant plumes become diluted by turbulence and baroclinic instability as they rise upwards
- In a transient phase, fresh oceans near the freezing point can develop bottom-hugging currents as warm fluid parcels contract on heating

Supporting Information:

Supporting Information may be found in the online version of this article.

Correspondence to:

S. Bire,
bire@mit.edu

Divergent Behavior of Hydrothermal Plumes in Fresh Versus Salty Icy Ocean Worlds

Suyash Bire[1] [ID], **Tushar Mittal[1,2]** [ID], **Wanying Kang[1]** [ID], **Ali Ramadhan[1]** [ID], **Philip J. Tuckman[1]**, **Christopher R. German[3]** [ID], **Andreas M. Thurnherr[4]** [ID], and **John Marshall[1]** [ID]

[1]Earth, Atmospheric, and Planetary Sciences, Massachusetts Institute of Technology, Cambridge, MA, USA, [2]Now at Department of Geosciences, Pennsylvania State University, University Park, PA, USA, [3]Woods Hole Oceanographic Institution, Woods Hole, MA, USA, [4]Lamont-Doherty Earth Observatory, Palisades, NY, USA

Abstract Water parcels close to their freezing point contract and become heavy on warming if they are sufficiently fresh (salinity less than 22g kg^{-1} for earth's ocean), but expand and become buoyant when salty (salinity greater than 22g kg^{-1}). We explore the resulting divergent behavior of hydrothermal plumes in fresh versus salty icy ocean worlds, with particular emphasis on Europa and Enceladus. Large, salty, putative Europa-like oceans, develop buoyant plumes which rise upwards in the water column when energized by localized hydrothermal vents. Instead, small, fresher, putative Enceladus-like oceans, can develop bottom-hugging gravity currents when heated near the freezing point, due to the anomalous contraction of fluid parcels on warming. Such a bottom-filling regime would most likely be a transient stage in the evolution of an icy moon over geological time. The contrasting dynamics are highlighted and rationalized in terms of key non-dimensional numbers with a focus on the ability of ocean to carry bio-markers from the hydrothermal activity at the bottom to the ice shell at the top. Finally, the implications of our study for prioritizing future missions to icy moons are discussed. An advantage of a mission to a large icy moon (e.g., Europa), rather than a smaller target (e.g., Enceladus), is that a larger moon's ocean would likely support buoyant convection, which could bring signatures of seafloor venting to the outer ice-shell regardless of that ocean's salinity. For smaller icy moons, the nature of convection would hinge on its assumed salinity.

Plain Language Summary Oceans on icy moons such as Enceladus and Europa may potentially have many of the conditions required for life. The possible existence of hydrothermal vents on the ocean floors of these moons are prime candidates as sources of biological activity. Here we explore the conditions in which heating at bottom vents might lead to convection that could carry biomarkers from the bottom of the ocean up to the ice. If the water is salty (perhaps Europa), upward-reaching plumy convection results which, if buoyancy fluxes are sufficiently large, can reach right up to the icy shell covering the ocean, allowing us, perhaps, to draw inferences about the interior ocean by observing the ice shell. If the background salinity is low, however, (perhaps Enceladus) heating close to the freezing point of water leads to dense, bottom-hugging density currents or very weak plumes. This will likely be a transient state in the evolution of the ocean of such a moon in which the bottom layer slowly warms up, but with much diminished communication between the bottom and the top. An advantage for any future mission to a large ocean world, is that it would likely host buoyant convection regardless of the ocean's salinity.

1. Introduction

Since the Cassini mission, Enceladus has become a prominent astrobiological target with potentially many of the conditions required for habitability (Cable et al., 2021; Glass et al., 2022; Hand et al., 2020). Enceladus is a member of a broader class of icy ocean worlds, a number of which may also be habitable (Nimmo & Pappalardo, 2016; Vance et al., 2018). Early observations of geological features on its ice shell led to speculations on the presence of an active subsurface ocean (Nimmo & Pappalardo, 2016). The subsequent discovery of plumes emanating from the south pole of Enceladus boosted the idea that Enceladus might possess a significant subsurface ocean (Hansen et al., 2006; Porco et al., 2006). Observations and modeling studies of exaggerated libration on Enceladus, along with gravity-topography analysis, have all but confirmed the presence of a global subsurface ocean with an average thickness of 35–45 km (e.g., Beuthe et al., 2016; Čadek et al., 2016; Hemingway & Mittal, 2019; Thomas et al., 2016; Van Hoolst et al., 2016). Additionally, studies of the composition of the plumes have indicated the presence of silica nanoparticles (Hsu et al., 2015; Sekine et al., 2015), hydrogen (Waite

et al., 2017), as well as salts and organic compounds (Fifer et al., 2022; Postberg et al., 2018). The actual salinity of the ocean is still a matter of debate.

Such observations are suggestive of active hydrothermal activity, with Enceladus's rocky core providing the thermochemical energy for potential life at/beneath the seafloor (Choblet et al., 2021). Furthermore, Choblet et al. (2017) show that if the porous rocky core (20%–30% porosity e.g., Hemingway and Mittal (2019)) is highly dissipative, core-scale porous media convection might focus hydrothermal activity at the poles. Rovira-Navarro et al. (2022) find qualitatively similar results for Enceladus's core using a poroviscoelastic rheology. However, viscous dissipation in the core can drive geological activity only if it has a low rigidity and viscosity. Choblet et al. (2017) also suggest, using scaling results from Goodman and Lenferink (2012), that hydrothermal heat localization could be sufficient to power hydrothermal plumes all the way up to the ice-ocean interface on a timescale of months.

In contrast to the aforementioned observational/porous flow modeling for Enceladus, most studies of convection or hydrothermal plume dynamics on icy moons have focused on Europa and/or have prescribed high seafloor heat fluxes (Ashkenazy & Tziperman, 2021; Bire et al., 2022; Goodman et al., 2004; Goodman & Lenferink, 2012; Soderlund et al., 2013). For example, Goodman et al. (2004) conducted laboratory experiments and derived scaling laws to predict the timescale over which plumes from the bottom of Europa's ocean would reach the surface. Additionally, they show that any given plume's life cycle would involve an initial transient stage during which the effects of planetary rotation are not felt, an intermediate stage in which the plume rises to the surface in columns, and a final stage in which the plume becomes baroclinically unstable and sheds secondary vortices. The main outcome was that predictions could be made about the efficiency of heat transfer from the sea floor to the base of the ice shell. Goodman and Lenferink (2012) tested these findings through numerical simulations, some of which are repeated here to ground the present study in previous results. They suggest that plumes could transport perhaps 0.1–10W m^{-2} from the seafloor to the base of the ice shell on Europa and span diameters of O(10 km).

A short-timescale paradigm provided the framework for the interpretation of geochemical measurements of plume particles on Enceladus (Choblet et al., 2017; Steel et al., 2017) and for the spectroscopy of surface material on Europa (Běhounková et al., 2021) and other icy ocean worlds. For example, Hsu et al. (2015) observe silica nanoparticles in plume ejecta from the south pole of Enceladus. Together with Sekine et al. (2015), they posit that particles originated from hydrothermal reactions in the rocky core and transited across the Enceladean ocean of thickness of O(10 km) in a matter of days to weeks. In order to match observational constraints on particle size, they also suggest that the salinity of the Enceladean ocean is less than 4% (or 40 g/kg). The fast transit-time paradigm is also behind attempts to explain various surface geological features and ice shell thickness variations on icy satellites (e.g., Čadek et al., 2019; Kvorka et al., 2018) using model results from solid core processes. Finally, an efficient transport from seafloor to ice shell (and potentially to the surface through jets or other cryovolcanism) is a key motivation for future space missions to these bodies in the search for extraterrestrial life, especially mission concepts that argue for landing on the ice shell and scooping surface material deposited by the plumes (Choblet et al., 2021; MacKenzie et al., 2022).

In all such discussions it is important to realize that the assumed salinity is a critical, but poorly constrained parameter. Most previous work assumes that the icy moon has a salty ocean with a salinity similar to Earth's ocean. With this assumption, seawater heated near its freezing point becomes lighter than the surroundings and hence rises. In contrast, at lower salinities (about half of Earth's ocean salinity), heating of water close to freezing temperatures, actually makes water denser, due to the anomalous expansion of near-freezing water (Ede, 1956; Ivanov & Nikolov, 2020). As first discussed by Melosh et al. (2004), if the ocean is sufficiently fresh a pool of increasingly warm but dense water can form at the base of the ocean and inhibit convection from directly reaching the upper light layer. If heat is continuously added from the core below, this state of affairs will likely only be a transient stage in the evolution of the oceans. Melosh et al. (2004) and Travis et al. (2012) suggest that eventually the layer would warm up sufficiently until the expansion coefficient becomes slightly positive. Previous work has also analyzed the role of salinity on the large scale circulation of icy ocean worlds and shown it to be a key parameter affecting the circulation (Kang et al., 2022; Zeng & Jansen, 2021). As argued by Kang et al. (2022), the most likely salinity for icy ocean worlds with shell thickness variation typical of Enceladus is of intermediate value (i.e., less than 20 g/kg, see later summary). This suggests that a very small (but perhaps not negative) thermal expansion coefficient is a real possibility for icy ocean worlds, either at present-day or earlier in their evolutionary history.

Our purpose here is to extend the studies of Goodman and Lenferink (2012) to parameter regimes appropriate to Enceladus. Additionally, we directly address the role of pressure and salinity in shaping the response of the ocean to hydrothermal heat sources in a parameter space of relevance to icy moons. In Section 2, we explore the equation of state (EOS) and the effect of salinity and pressure on the thermal expansion coefficient of seawater. The numerical simulations designed to study hydrothermal plume dynamics in nominally Enceladus-like and Europa-like icy moons as well as relevant non-dimensional numbers are described in Section 3. Sections 4 and 5 contrast the behavior of hydrothermal plumes in the cases where the thermal expansion coefficient is positive and negative, respectively. Section 6 discusses the implications of our study for various icy moons and in the planning of future missions to explore them.

2. Thermal Expansion Coefficient of Water

One of the key variables that determines the dynamics of hydrothermal plumes is the thermal expansion coefficient of water since this controls the buoyancy of fluid parcels upon heating. The thermal expansion coefficient of water depends on, amongst other things, the amount and type of dissolved solute. Early estimates of the salinity of Enceladus' ocean were based on assumptions of thermodynamic equilibrium. Considering a range of hydrothermal and freezing conditions for chondritic compositions, an ocean in equilibrium with the rocky core will have a present day salinity of between 2 and 20 g/kg (Glein et al., 2018; Zolotov, 2007; Zolotov & Postberg, 2014). However, at least ~17 g/kg may be required to keep the geysers' liquid–gas interface convectively active ensuring that they do not freeze up (Ingersoll & Nakajima, 2016). Sodium-enriched samples taken by Cassini from south pole sprays suggest an ocean salinity of 5–20 g/kg. This can be considered a lower bound since the interaction of cold water vapor sprays with their environment may lower the salinity of droplets through condensation (Postberg et al., 2009). There is also considerable additional uncertainty since fractional crystallization and disequilibrium chemistry may partition components in such a way that geyser particles are not directly representative of the underlying ocean (Fox-Powell & Cousins, 2021). Furthermore, if particles originate from a hydrothermal vent, their composition can deviate far from that of the overall ocean (Fifer et al., 2022; Glein et al., 2018). It is of note that the size of silica nano-particles carried along in the sprays has also been used to estimate ocean salinity. Assuming an intermediate value of pH and a short transport timescale induced by hydrothermal activity, a salinity <40 g/kg is obtained (Hsu et al., 2015). In a separate line of argument, oceans with too much or too little salt may have a strong ice pump effect, leading to the erosion of ice thickness gradients (Kang et al., 2022). In conclusion, the ocean salinity of Enceladus can have a large, observationally permissible range. Europa's ocean salinity is even more poorly constrained. The amplitude of the magnetic induction signal suggests a rather salty (>50 g/kg), deep ocean. However, significant degeneracy exists in the retrieval process (Hand & Chyba, 2007) and there is uncertainty about the effect of accreted volatiles (CO_2, NH_3) on ocean conductivity.

The specific chemical composition of the oceans inferred from Enceladus' south polar plume is also an ongoing field of study (Fifer et al., 2022; Glein et al., 2018; Khawaja et al., 2019; Postberg et al., 2022). Sodium chloride inferred from plume measurements yields information about the salinity of the ocean on Enceladus (Glein et al., 2018; Postberg et al., 2009). Spectroscopy of the plumes has also indicated the presence of ammonia (Waite et al., 2017), along with other volatile species. The composition of Europa's ocean is similarly uncertain. Trumbo et al. (2019) report evidence for sodium chloride on Europa's ice crust. Moreover, modeling studies of composition of Europa's ocean suggest that it might be enriched in metallic salts such as magnesium sulfate (Vance et al., 2018). Given the distinct initial state and evolutionary history of icy moons, the composition of seawater therein could be very distinct from that on Earth. Given the large plausible parameter space for ocean salinity and composition for icy ocean worlds, it is not clear that the terrestrial EOS near the freezing point of water is the most relevant. Given these possibilities, we now briefly explore the range of likely thermal expansion coefficients of water under varying temperatures, pressures, and compositions.

We first contrast the thermal expansion coefficient of the near-surface ocean on Enceladus (Figure 1a) with that of Europa (Figure 1e), assuming that an EOS for NaCl dominated water such as that on Earth's ocean (TEOS-10) is appropriate (Millero et al., 2008; Roquet et al., 2015). Similarly, in panels b and f we also plot the likely variation of the thermal expansion coefficient on Enceladus and Europa assuming a magnesium sulfate solute using the *PlanetProfile* algorithm (Vance et al., 2014). We also compare the thermal expansion coefficient of the deep (pressurized) ocean on Enceladus and Europa in panels c and g using the seawater EOS and in panels f and h using the EOS for water rich in magnesium sulfate.
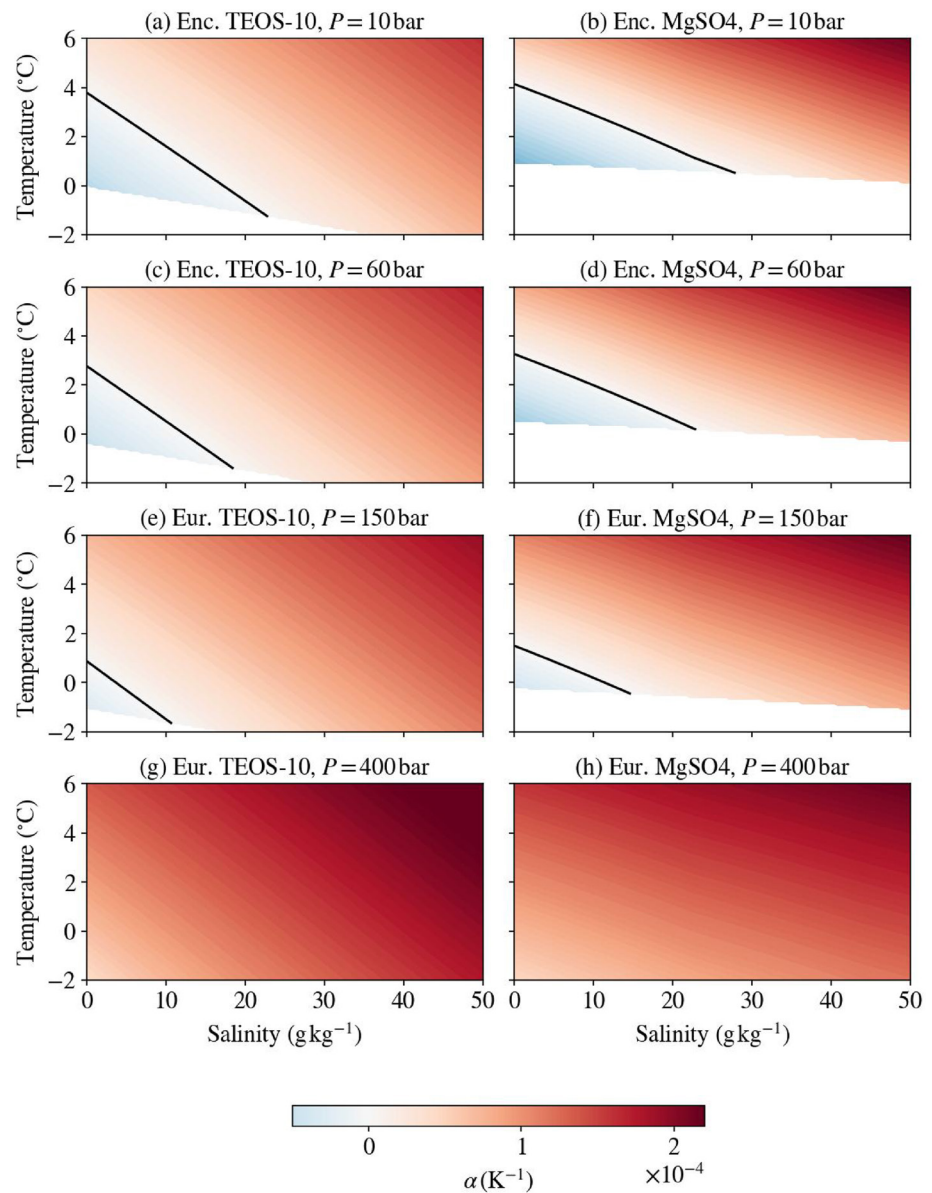
Figure 1. The thermal expansion coefficient of seawater at pressures of (a) 10, (c) 60, (e) 150, and (g) 400 bar is shown in the first column. Similarly, that of water rich in magnesium sulfate is shown in the second column in panels (b, d, f, and h). The pressures of 10 and 60 bar roughly correspond to depths of 5 and 50 km, respectively, on Enceladus, while 150 and 400 bar roughly correspond to depths of 5 and 30 km on Europa. The region in white indicates temperatures below the freezing point. Thermal expansion coefficient changes sign across the black line. The figure in panel (a) is similar to that in Zeng and Jansen (2021).

The first pattern to note in all the panels is that the thermal expansion coefficient at any given temperature and pressure increases with the concentration of salt. The presence of ionic compounds in water disrupts hydrogen bonding and causes it to expand on heating (Ede, 1956; Ivanov & Nikolov, 2020). Thus, at high concentrations of salts, the thermal expansion coefficient of ocean water is always positive. However, at low salt concentrations, we do see negative values of α for temperatures below ~4°C in panels a, b, c and d. Thus, fresher oceans result in anomalous behavior in which water close to freezing becomes denser upon heating.

A second pattern can be seen in Figure 1: panels e, f, g, and h show that negative values of thermal expansion coefficient are only attained at very low values of pressure on Europa. This behavior results from non-linearities in the equation of state and especially their sensitivity to pressure. Since Europa's gravity is about 10 times
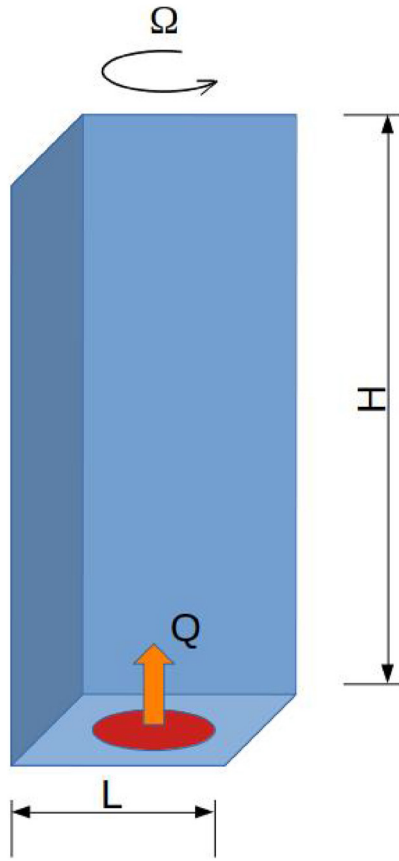
Figure 2. The configuration of the numerical model. The domain size is $10 \times 10 \times 40$ km^3. A heating patch is applied at the bottom with an area of 1×1 km^2 shown in red which acts as the source of the hydrothermal plume. The resolution of the model is 40 m in the horizontal and 80 m in the vertical.

stronger than that of Enceladus, pressure increases more rapidly with depth on Europa. Assuming ice shell thickness on Enceladus and Europa to be 30 and 10 km, respectively, the hydrostatic pressure at a depth of 5 km from the base of the ice shell on Enceladus is 10 bar while that on Europa is 150 bar. This difference becomes larger the deeper we go. Therefore, in panels g and h, we see that high pressures at deeper levels in Europa's ocean suppress anomalous contraction of water under warming.

A key conclusion of our EOS survey is that for high salinity Europa-like oceans, the effect of salinity is not likely to suppress buoyant, plumy dynamics triggered by bottom heating. This is true regardless of whether the ocean is dominated by chloride or sulfate salts or high ammonia concentrations. On the other hand, in the case of Enceladus, typical values of salinity estimated from previous studies (~10–20 g/kg) (Hsu et al., 2015; Kang et al., 2022) can place it in the region of negative alpha. While large concentrations of ammonia lead to a positive thermal expansion coefficient, small amounts can still lead to a negative limit for alpha (not shown). This is especially important for Enceladus since best current estimates of ammonia concentrations there are 4–13 g kg^{-1} (assuming seawater composition is the direct volume mixing gas abundance ratios in the plume) (Waite et al., 2017) and 0.1–2 g kg^{-1} when accounting for fractionation of gas plume composition due to water vapor condensation and gas exsolution (Fifer et al., 2022). At such concentrations, especially when accounting for gas fractionation, Enceladus's ocean could indeed be in the negative alpha regime.

3. Numerical Explorations of Hydrothermal Plumes on Fresh Versus Salty Icy Ocean Worlds

3.1. Experimental Design

We employ *Oceananigans.jl*, a state-of-the-art non-hydrostatic ocean circulation model based on the MITgcm (Marshall et al., 1997) but written in Julia to run fast on graphical processing units (Ramadhan et al., 2020), configured for study of hydrothermal plumes at high-resolution. The domain stretches from 0 to L in both zonal (x) and meridional (y) directions and from $z = -H$ to $z = 0$ in the vertical direction as shown in Figure 2. In our Enceladus control experiment, L and H are set to 10 and 40 km, respectively. The grid is rectilinear with a spacing of 40 m in the horizontal and 80 m in the vertical. For our experiments using Europa-like parameters, L is extended to 40 km and the horizontal grid spacing is coarsened to 80 m. Additionally, we recreate some simulations from Goodman and Lenferink (2012) using an isotropic grid resolution of 500 m to place our experiments in the context of previous work. Our results are not sensitive to domain size as long as it is sufficient to prevent self-interaction of plumes across our periodic boundary conditions.

In our Enceladus-like runs, the horizontal and vertical Laplacian diffusivity is set to 2.5×10^{-3} m^2 s^{-1} and 10^{-2} m^2 s^{-1}, respectively, large enough to ensure numerical stability but small enough to allow turbulent convection to ensue. The Prandtl number is 1. These choices do not affect key conclusions of our study.

At the bottom, $z = -H$, a patch of heating is prescribed thus:

$$Q = Q_0 \exp\left[-\frac{(x - x_0)^2 + (y - y_0)^2}{2\,\sigma^2}\right], \tag{1}$$

where $x_0 = y_0 = L/2$ is at the center of the domain and $\sigma = l/\sqrt{2\pi}$ controls the width of the patch. The choice of l and Q_0 controls the magnitude of the implied seafloor heat flux and its degree of localization. The total heat flux entering the domain is

$$E = \iint Q \, \mathrm{d}x \, \mathrm{d}y = Q_0 \, l^2. \tag{2}$$

Table 1
Summary of Experimental Parameters: Gravity g = (1.3, 0.1) ms⁻² Corresponding to, Nominally, Europa (Top Rows) and Enceladus (Bottom Rows), Thermal Expansion Coefficient α, Reference Salinity S, Rotation Rate Ω, Domain Width L, Depth H, Viscosity ν, Grid Spacing in Horizontal and Vertical Directions Are dx and dz, Heat Flux Maximum Q_0, Parameter $l = \sqrt{2\pi}\sigma$ Controlling the Lateral Scale of the Heating Patch (Equation 1), Total Heat Flux E (Equation 2), Buoyancy Flux F (Equation 3), Rotational Length Scale l_{rot} (Equation 6) and Natural Rossby Number Ro*(Equation 7)

	G (m s⁻²)	α (10⁻⁴ K⁻¹)	S g kg⁻¹	Ω (10⁻⁵ s⁻¹)	L (km)	H (km)	ν (10⁻³ m² s⁻¹)	dx (m)	dz (m)	Q_0 (W m⁻²)	L (km)	E (10⁻² GW)	F (10⁻⁵ m⁴ s⁻³)	l_{rot} (m)	Ro^* (10⁻³)
+	1.3	3.0	35	1.0	40	40	2.5	80	80	1	1	0.1	9.11	327	8.2
⊕	1.3	3.0	35	1.0	40	40	2.5	80	80	100	1	10	911	1,033	25.8
×	1.3	3.0	35	1.0	128	50	90.0	500	500	10,000	1	1,000	9.11×10^4	3,267	65.3
○	1.3	3.0	35	1.0	128	50	90.0	500	500	100	1	10	911	1,033	20.7
●	1.3	3.0	35	1.0	128	50	90.0	500	500	10	1	1	91.1	581	11.6
†	1.3	3.0	35	1.0	128	50	90.0	500	500	1	1	0.1	9.11	327	6.5
◁	1.3	3.0	35	1.0	128	50	1.0	500	500	10	1	1	95.9	588	11.8
▷	1.3	3.0	35	1.0	128	50	1.0	500	500	1	1	0.1	9.59	331	6.6
⊞	0.1	0.1	35	5.3	128	40	90.0	500	500	100	1	10	2.45	67	1.7
⊘	0.1	0.1	35	5.3	10	40	2.5	40	79	100	1	10	2.45	67	1.7
⊖	0.1	0.1	35	5.3	10	40	2.5	40	79	1,000	1	100	24.5	120	3.0
⊗	0.1	0.1	35	5.3	10	40	2.5	40	79	10	3	9	2.2	66	1.6
▽	0.1	−0.1	15	5.3	10	40	2.5	40	79	100	1	10	−2.45	67	1.7

Note. In all calculations the specific heat capacity is set to 4,000 J kg⁻¹ K⁻¹. Values of F, l_{rot}, and Ro^* for the fresh ocean, ▽, are calculated using a linear equation of state with $\alpha = -0.1$ K⁻¹. Runs in rows 1 to 8 are similar to those in Goodman and Lenferink (2012).

Table 1 summarizes all simulations carried out in our study, their associated parameters and non-dimensional numbers. It should be noted that in most of our experiments (first 12 rows) we have a positive α appropriate for a salty ocean with $S = 35$g kg⁻¹. We employ a linear equation of state for these 12 experiments. We also explore convection in a fresh ocean with $S = 15$g kg⁻¹ with a negative α in experiment ▽, which uses the 55 term polynomial approximation to the TEOS-10 proposed by Roquet et al. (2015). We also repeated experiment ⊘ with the same TEOS-10 by setting $S = 35$g kg⁻¹—not shown—yielding results that are virtually indistinct from ⊘. Note that the Roquet et al. (2015) formulation is highly calibrated to Earth's oceans and may not be a good description for icy moons, as discussed in Section 2. We scale the pressure used in it by the ratio of the gravity of Enceladus to that of Earth.

In our control Enceladus experiment (marked ⊘ in Table 1) we set l to 1,000 m and Q_0 to 100W m⁻² yielding $E = 10^8$W $= 0.1$ GW coming in over an area of 10×10 km². The average value over the entire domain is 1W m⁻². If we integrate this average value over the surface area of Enceladus's ocean floor, we get a net heat input of about 500 GW. This is ∼10–20 times that suggested by Choblet et al. (2017) indicating that we are applying even more heat than suggested by them.

Our Europa-like control experiment (marked ⊕ in Table 1) has exactly the same heat flux as that in our control Enceladus experiment, that is a Q_0 of 100W m⁻² and $l = 1,000$ m, again yielding $E = 0.1$ GW. The domain size of the Europa experiment, however, is larger and the average heat flux over the entire domain is 62.5 mW m⁻². Integrating this average value over the entire surface area of Europa gives a net heat input of about 1600 GW. This value is about twice that suggested by Běhounková et al. (2021).

Before going on it should be stated that the form and amplitude of the heat flux disk acting as a source of buoyancy for hydro-thermal plumes are rather uncertain. Our belief is that what matters at first order for the bulk response of the fluid to a "localized" heating patch—but not the detailed dynamics—is the integrated buoyancy flux F, or equivalently, the integrated power E. The details must matter to some degree, however. One can anticipate that the response of the ocean to a uniformly distributed source over the whole of the moon would be very different from one in which the heat input was very localized in space. This has been explored in the case of open-ocean deep convection—see Legg and Marshall (1993). There the authors find that the scale of the patch relative to the deformation radius determines the clumping scale of the plumes by baroclinic instability.

3.2. Key Non-Dimensional Numbers

In order to place our study in the context of previous work, we review key non-dimensional parameters and scaling results from Goodman and Lenferink (2012). We first define a buoyancy flux with units of $m^4 \, s^{-3}$ integrated over the horizontal domain,

$$F = \iint B \, dx \, dy, \tag{3}$$

where

$$B = \alpha g \frac{Q}{\rho_0 C_P}, \tag{4}$$

is the local buoyancy flux in $m^2 \, s^{-3}$. A parcel under the action of buoyancy, F, convectively rises. Its evolution can be characterized by the scales,

$$l \sim \left(F \, t^3 \right)^{1/4}, \quad u \sim w \sim \left(\frac{F}{t} \right)^{1/4}, \quad g' \sim \left(\frac{F}{t^5} \right)^{1/4}, \tag{5}$$

where t is time. For processes influenced by the rotation of the moon, we can substitute t with f^{-1}, where $f = 2\,\Omega$ is the rotation rate of the moon, which gives the rotational length scales,

$$l_{\text{rot}} \sim \left(\frac{F}{f^3} \right)^{1/4}, \quad u_{\text{rot}} \sim w_{\text{rot}} \sim (F \, f)^{1/4}, \quad g'_{\text{rot}} \sim \left(F \, f^5 \right)^{1/4}. \tag{6}$$

These scales have been invoked before to study convective plumes in a rotational regime—for example Fernando (1991), Jones and Marshall (1993), Helfrich (1994), Maxworthy and Narimousa (1994), Speer and Marshall (1995), Goodman et al. (2004), Goodman and Lenferink (2012), and Bire et al. (2022). A non-dimensional number, the natural Rossby number,

$$Ro^* = \frac{l_{\text{rot}}}{H} = \frac{1}{H} \left(\frac{F}{f^3} \right)^{1/4}, \tag{7}$$

can be devised from these scales, where H is the depth of the fluid. The length scale, l_{rot} is a measure of the distance a buoyant parcel of fluid travels in a rotation period. Thus, the natural Rossby number can essentially be thought of as a ratio of two length scales, l_{rot} and H; if the ratio is small the depth of the ocean is much larger than the distance traveled by a heated parcel in 1 day, while if the ratio is large the parcel reaches the surface at height H before rotation can influence its motion. As discussed in Bire et al. (2022), Ro^* has great utility because it only depends on externally prescribed parameters which are somewhat constrained by observations and is independent of uncertain eddy viscosities and diffusivities which are set by the nature of unresolved and unobservable small-scale turbulence.

The convective velocity and buoyancy scales from Equation 6 can be written in terms of the natural Rossby number:

$$\frac{w_{\text{rot}}}{f \, H} \sim Ro^*, \quad \frac{g'_{\text{rot}}}{f^2 \, H} \sim Ro^*. \tag{8}$$

In addition to Ro^*, other key paramaters of our experiments are the Ekman number, $E_k = \nu/(fH^2)$, and the Prandtl number $P_r = \nu/\kappa$, where κ is the thermal diffusivity. We set the $P_r = 1$ and, for the parameters in Table 1, a typical Ekman number is 6×10^{-8}, a relatively small value compared to previous studies. Note also from Table 1, that Ro^* is very much smaller on Enceladus than it is on Europa even if the heat fluxes are assumed to be the same. This is because g and α are much smaller on Encleadus than Europa and the buoyancy flux, Equation 4 which involves the product $\alpha \times g$, is accordingly very much smaller. This is the key to understanding the fundamental differences between buoyant hydrothermal convection driven from below on the two icy moons.

4. Buoyant Plumes in Saline Oceans

In the spirit of Goodman and Lenferink (2012) we perform the series of numerical simulations outlined in Table 1. Those with a gravity of $g = (1.3, 0.1) \, ms^{-2}$ and $\Omega = (5.3, 1.0) \times 10^{-5} \, s^{-1}$ correspond to, nominally, Europa and

Enceladus. They are separated out in Table 1, Europa on top and Enceladus on the bottom. Each simulation is initiated from a state of rest when a heated patch is turned on at the bottom boundary.

We begin by describing the experiment shown in Figure 3—marked $\oplus$ in the table—which is similar to one of the prominent examples in Goodman and Lenferink (2012) focusing on Europa, albeit here at higher resolution. The salinity is set to $S = 35 \mathrm{g\,kg}^{-1}$. The plume rises to the surface very rapidly, in about ~15 days. Since buoyant water is continually supplied from the seafloor, the main vortex fills up, undergoes baroclinic instability and splits into individual vortices which spread horizontally. To place our results in the context of Goodman and Lenferink (2012), we redid a series of such experiments motivated by their study—see below.

Figure 4 shows typical characteristics of a plume originating from a bottom-heated patch in a salty ocean in which again $S = 35 \mathrm{g\,kg}^{-1}$ but with parameters more typical of Enceladus—this is the saline Enceladus case, $\oslash$, from Table 1. Note that buoyancy fluxes are much smaller than in the Europa case because of the small value of gravity on Enceladus. The temperature and particles released into the flow, as shown in panels b, c, j, and k, indicate that the influence of the bottom heating patch is to create plumes which rise to a height of roughly 10 km from the seafloor after 400 rotation periods or so. Plan views of horizontal and vertical currents and temperatures shown in panels d to i, reveal that swirling currents and eddies are created which sweep warm fluid laterally (via baroclinic instabilities), not just vertically, away from the heating source. It is for this reason that in this lower buoyancy flux case, plumes do not reach all the way up to the surface, even after integrating for hundreds of rotation periods. Rather the influence of the heating patch is very efficiently spread out laterally.

In summary then, our Europa-like plumes push up to the surface rapidly, in a few 10s of days. By contrast, our Enceladus-like plumes become baroclinically unstable before they reach the upper boundary and the influence of the seafloor is felt by the ice shell on timescales of years rather than days. The key to understanding these differences is to appreciate the role of rotation and baroclinic instability, as captured by $Ro*$.

In simulations in which $Ro*$ is sufficiently small, plumes come under rotational control and vertical speeds are given by Equation 8. Support is found in Figure 5a where vertical velocity associated with the plumes, w', from our suite of experiments is plotted against $Ro*$: points cluster around a slope of unity. Moreover, the vertical scale to which the plumes reach before baroclinic instability arrests their upward thrust—which we call h—is given by $h \sim w_{rot}/f = l_{rot}$ or, equivalently, $h/H \sim Ro*$. Details of how we compute h from our experiments is given in Supporting Information S1. Figure 5b lends support to these ideas and shows that as $Ro*$ becomes smaller the vertical scale to which localized convection gives way to lateral mixing due to baroclinic instability also becomes smaller. As $Ro*$ increases, in contrast, h/H approaches unity and plumes rise directly up to the ice shell.

On comparing Figure 5a with those of Goodman and Lenferink (2012)—see their Figure 6—our simulated speeds are in broad agreement. However, we find a better agreement with the rotational scaling (u_{rot}) than with the cone scaling (u_{cone}). The latter was preferred by Goodman and Lenferink (2012) for their plumes which reached all the way to the ice shell. At low $Ro*$ plumes do not reach the upper boundary and spread laterally more than vertically. Furthermore, none of their simulations were integrated beyond 20–25 rotation periods, and so it is possible that our scales at low Rossby number may be representative of a much later stage that was not explored by them.

One important implication of Figure 5, is that if $Ro*$ is indeed small, then the geometrical details of the assumed heating patch at the bottom are mixed away laterally by baroclinic instability. If, however, $Ro*$ is sufficiently large, then the heating patterns can be projected across the fluid to the very top. The latter is the limit considered by Goodman and Lenferink (2012) for Europa—the former is the appropriate limit for Enceladus, we believe, as now discussed.

Enceladus, due to its small gravity and tiny thermal expansion coefficient, typically has very weak buoyancy forcing, F, (even after prescribing an order-of-magnitude more localization than suggested by Choblet et al. (2017)) and a very small value of $Ro*$, roughly commensurate with the $Ro*$ pertaining to the experiment $\oslash$ shown in Figure 4. This should be contrasted with Europa which, due to its larger gravity and larger expansion coefficient, has an F which is almost three orders of magnitude larger shown by $\oplus$. Europa is also thought to be a considerably deeper ocean than Enceladus. These factors lead to an $Ro*$ on Europa which is 10 times larger than that on Enceladus, although it remains much smaller than unity.

Note that for the parameters assumed in Figure 3, representative of a high heat flux end-member for Europa, F is more than 100 times larger than is perhaps reasonable, given the heat fluxes estimated by Běhounková
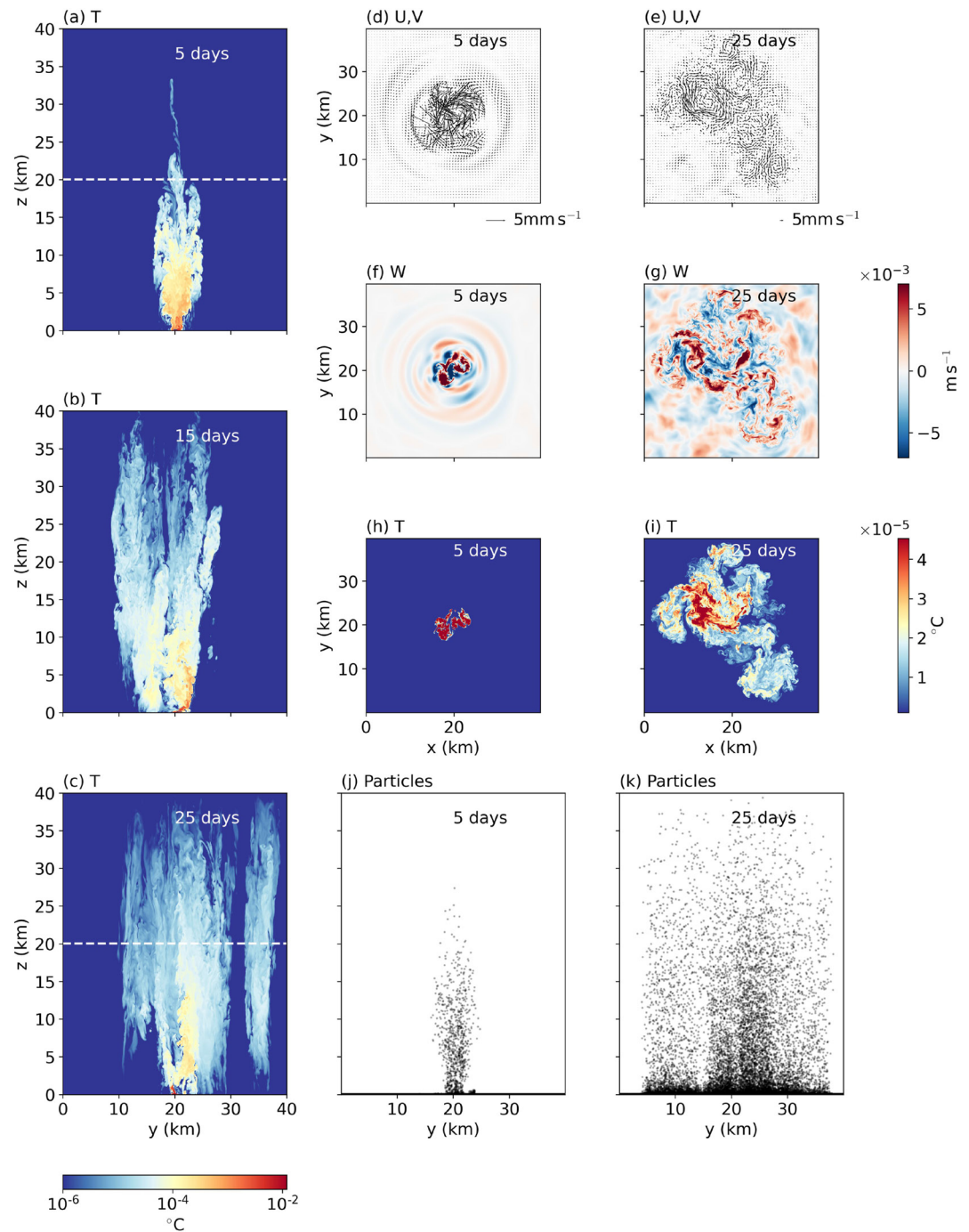
Figure 3. Panels a, b, and c show the meridional sections of temperature at $x = 20$ km due to a hydrothermal plume for a saline ocean at 5, 15, and 25 rotation periods, respectively. Panels d and e show the velocity vectors 20 km above the bottom at 5 and 25 rotation periods, respectively. Panels f and g show the vertical velocity at 5 and 25 rotation periods, respectively. Panels h and i show the plan view of temperature 20 km above the bottom at 5 and 25 rotation periods, respectively. Panels j and k show the meridional sections at $x = 20$ km of particles initially released at the bottom. This is the Europa-like case, ⊕, from Table 1. Animations are provided in Movies S1–S6.

et al. (2021), and $Ro*$ order 10 times larger. In this case a plume rising from (and particles released from) a hydrothermal vent at the bottom travels all the way to the ice shell in several 10s of days. In these high Rossby number experiments, plumes reach the ice shell before spreading horizontally. At low Rossby numbers by contrast, as in Figure 4, plumes disintegrate before reaching the ice shell and shed secondary vortices which spread horizontally.
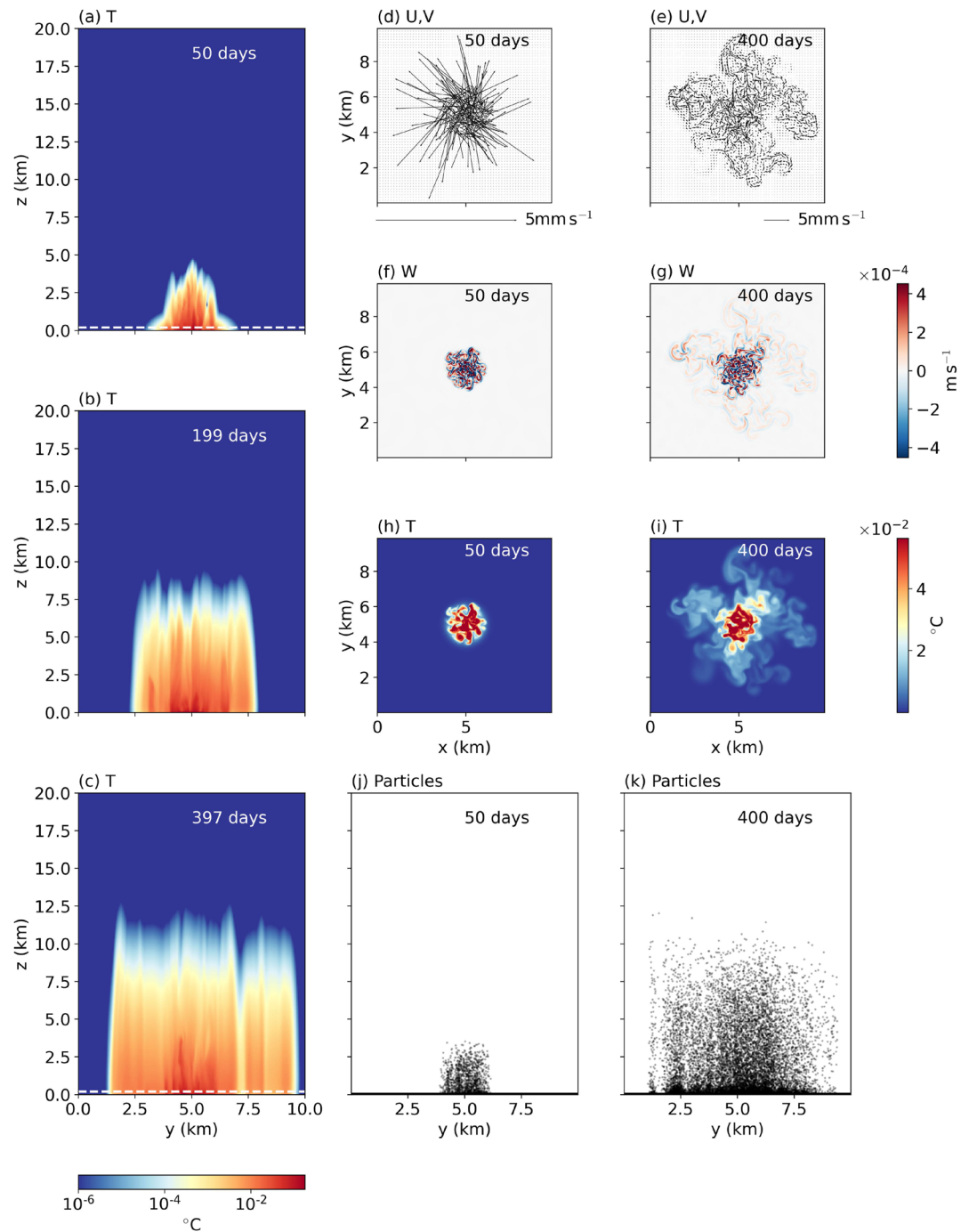
Figure 4. Panels a, b, and c show the meridional sections of temperature at $x = 5$ km due to a hydrothermal plume for a saline ocean at 50, 200, and 400 rotation periods, respectively. Panels d and e show the velocity vectors 80 m above the bottom at 50 and 400 rotation periods, respectively. Panels f and g show the vertical velocity at 50 and 400 rotation periods, respectively. Panels h and i show the plan view of temperature 80 m above the bottom at 50 and 400 rotation periods, respectively. Panels j and k show the meridional sections at $x = 5$ km of particles initially released at the bottom. This is the saline Enceladus case, ⌀, from Table 1. Animations are provided in Movies S1–S6.

Due to the finite lateral size of our domain and the use of periodic boundary conditions, these vortices can self-interact: warm water begins to rise slowly and diffusively throughout the entire water column. In order to understand the long time-scale dynamics, a larger domain size would be required—see the discussion in the conclusions.
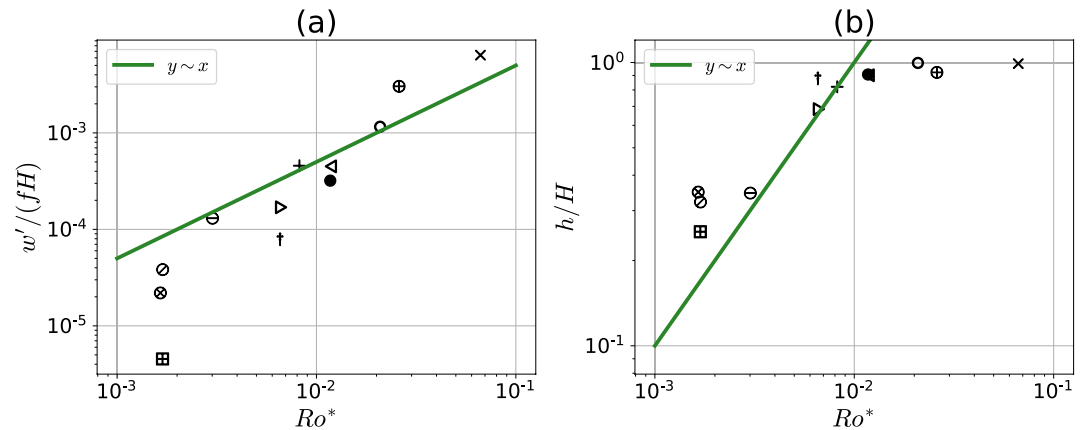
Figure 5. (a) Vertical velocity associated with the plumes, w', non-dimensionalized by fH as a function of Rossby number. The line has a slope of unity as implied by the scaling given by Equation 8. (b) The ratio of the plume height at which baroclinic instability, h, occurs to the depth of the domain as a function of Rossby number. The line has a slope of unity. See Supporting Information S1 for how w' and h are calculated.

5. Bottom Spreading Gravity Currents in Fresh Oceans

The ocean on Enceladus is close to freezing and, if sufficiently fresh, α and hence the buoyancy flux, could be negative. Figure 6 shows typical flow patterns of plumes heated in a fresh ocean near freezing temperatures in which the salinity is set to 15g kg^{-1} and α is indeed negative—experiment ∇ in Table 1. In this case, the water directly above the heating patch initially becomes warm and dense. As shown in Figure 6, continuous heating provides an uninterrupted supply of dense water which spreads radially outwards along the bottom. A few rotation periods after commencement of heating, the dense current comes under the influence of rotation and forms an anticyclonic circulation around the source (heating patch) as can be seen in Figure 6d. Eventually, as more and more dense water is supplied, the outflow forms four secondary vortices (panels e, g, i). The temperature signature and particles released at the bottom seen in panels c and k, respectively, further show that the plume does not become buoyant and rise in the water column, at least in the first 400 rotation periods.

Continuously forced gravity currents have not been extensively studied but there is some relevant literature on lock release experiments (e.g., Dai & Wu, 2016, 2018; Griffiths & Linden, 1981; Saunders, 1973). Typically, they involve releasing a fluid of higher or lower density into ambient fluid in a rotating system. If dense fluid is released it naturally settles at the bottom, while if the released fluid is light, it rises to the top. In the former case, the dense fluid is affected by bottom friction but otherwise the two cases are rather similar to one-another (Saunders, 1973).

The difference in density provides a parameter known as the reduced gravity or buoyancy given by

$$g' = g\frac{\rho_1 - \rho_0}{\rho_0} = -b,\tag{9}$$

where g is the acceleration due to gravity and ρ_0 is the density of the background fluid and ρ_1 is that of the released fluid. A critical parameter is the Rossby radius of deformation,

$$l_\rho = \frac{\sqrt{g'H}}{f},\tag{10}$$

where H is the depth of the fluid. This is the lateral scale at which the propagating gravity waves are influenced by rotation. In the lock release experiments, the ratio of l_ρ to that of the scale of the cylindrical release lock, R is

$$B_u = \frac{l_\rho^2}{R^2},\tag{11}$$

and defines a non-dimensional (Burger) number B_u. For low values of B_u the outflow splits up into rotationally controlled vortices described by Saunders (1973). For intermediate values, a vortex forms around the lock but never detaches from it. For high values of B_u the radial outflow does not feel rotation and is diverted in the azimuthal direction forming a "bulbs-and-wedges" pattern on the outer periphery (Dai & Wu, 2016, 2018).
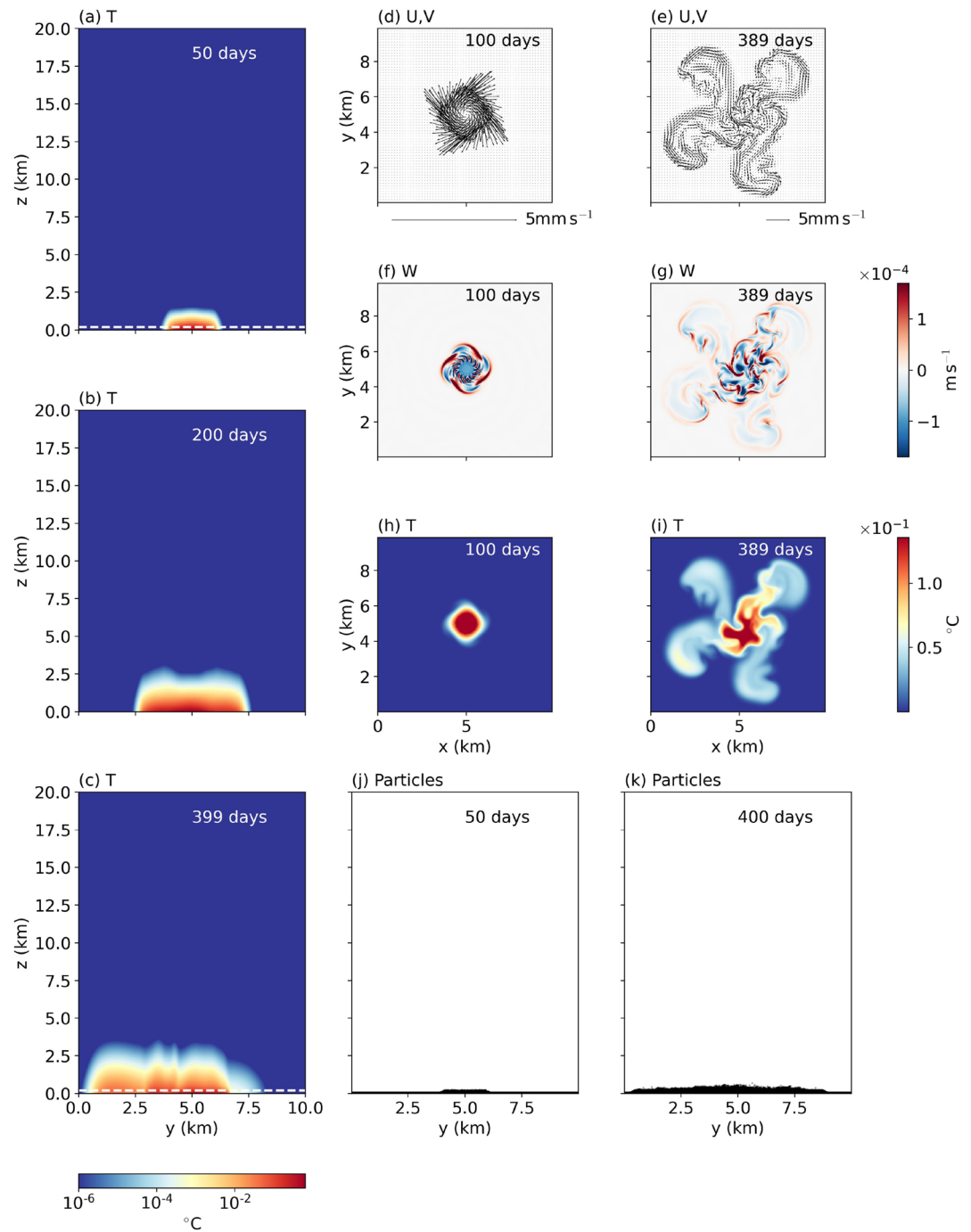
Figure 6. Panels (a–c) show the meridional sections of temperature at $x = 5$ km due to a hydrothermal plume for a fresh ocean at 50, 200, and 400 rotation periods, respectively. Panels d and e show the velocity vectors 80 m above the bottom at 50 and 400 rotation periods, respectively. Panels (f and g) show the vertical velocity at 50 and 400 rotation periods, respectively. Panels h and i show the plan view of temperature 80 m above the bottom at 50 and 400 rotation periods, respectively. Panels j and k show the meridional sections at $x = 5$ km of particles initially released at the bottom. This is the fresh Enceladus case, ∇, from Table 1. Animations are provided in Movies S1–S6.

Griffiths and Linden (1981) performed laboratory experiments in which they compared constant volume lock-release with constant flux cases (fluid is released at the top at a constant rate more akin to our numerical experiments). In the constant flow rate case, they find that the light fluid spreads at the surface initially for ~1–2 rotation periods after which baroclinic instability develops on the near vertical interface between the light and

dense fluid for the case of low B_u. The baroclinic instability is initially small but grows with time and imparts a non-axisymmetric nature to the flow. The non-axisymmetric component of the flow eventually grows to shed independent vortices from the main initial vortex. The number of new vortices shed again depends on the ratio of Coriolis to buoyancy forces, as well as on the depth occupied by the injected flow. This behavior is qualitatively similar to results from our experiment in which the Rossby radius of deformation is order 100s of m and hence much smaller than the domain size (R), leading to a small value of B_u and hence vortex splitting.

Although Griffiths and Linden (1981) characterized an empirical relationship between the number of secondary vortices and non-dimensional parameters such as B_u, their domain was horizontally constrained and boundary effects became significant. In addition, in their experiments, the depth of the injected flow may have become comparable to that of the Ekman layer leading to substantial viscous effects. Both Saunders (1973) and Griffiths and Linden (1981) find that viscous effects facilitate secondary vortex formation in surface as well as bottom Ekman layers. Thus, further research needs to be undertaken to understand the nature of vortex splitting in the constant flux case and the effect of Ekman layers and bottom friction on flow instability.

Nevertheless, our results, when combined with existing work on forced gravity currents, suggest that hydrothermal activity in a fresh, cold ocean are likely to lead to the formation of unstable vortices of dense fluid running over the seafloor. This scenario is very different from the plumy convection observed on heating a fluid in which the thermal expansion coefficient is positive. The $15\,\mathrm{g\,kg^{-1}}$ salinity adopted here has been chosen for illustrative purposes. In the real Enceladean ocean, if the salt composition and concentration results in anomalous contraction of water on heating, the bottom spreading case could occur.

Melosh et al. (2004) first postulated that a bottom gravity current scenario might be appropriate for Europa. They argued that even in a fresh ocean, the accumulation of warm water at the bottom would eventually trigger convection because the temperature would rise and, along with it, the associated thermal expansion coefficient until it became positive. They suggested that a vertical structure would be set up in which a convective bottom layer would be capped by a stably stratified "stratosphere" in which diffusive mixing would be operative. We concur that bottom-spreading may be a transient phase in the evolution of Enceladus over "geological" times, depending on the duration and intensity of hydro-thermal activity. Today's Enceladus might be closer to the two-layer structure envisaged by Melosh et al. (2004) and Zeng and Jansen (2021). However, it should be noted that the thermal expansion coefficient in the bottom convective layer might be positive but vanishingly small due to convection triggering transport of warm water upwards and away as soon as it becomes buoyant. High pressures at the bottom of Enceladus are also conducive to small α's, as noted in Vance et al. (2018) and Soderlund (2019). This will lead to smaller buoyancy anomalies and weaker plume activity characteristic of low $Ro*$ as discussed in Section 4. Therefore, irrespective of whether Enceladus is presently past this transient stage, hydrothermal plumes from its seafloor may likely not leave their imprint on its ice shell.

If a fresh Enceladus were assumed to be in a transient stage in which the bottom layer had a negative thermal expansion coefficient, "dense" hydrothermal activity would ensue with heavy fluid flowing out from venting systems hugging the bottom. Owing to the resulting stable stratification and a steady supply of minerals from the core, the bottom dense layer could become chemically enriched. This mineral-rich dense layer and its interface with the lighter layer above, could potentially provide rich habitats for chemosynthetic life away from any liquid-solid interface such as the base of the ice shell or the seafloor. It has long been known that chemosynthetic microbial activity can occur at chemical gradients in mid-water away from any liquid-solid interface, as described at redox interfaces in anoxic basins such as the Black Sea and Saanich Inlet since the 1980s (Tebo et al., 1984). The same processes are now recognized to also be present across large swathes of Earth's deep ocean basins within oxygen minimum zones, for example, across much of the Eastern Tropical Pacific Ocean and across the Arabian Sea in northern Indian Ocean where a diversity of microbial metabolic niches are sustained. Since the Enceladus' rocky core likely has high porosity (Choblet et al., 2017), the dense hydrothermal fluid could also strongly affect the porous flow in the core by enhancing fluid flow into the core. This could provide an additional mechanism to stimulate chemically fueled microbial activity in a deep sub-seafloor biosphere on Enceladus—an area of research that is of particular current interest here on Earth (Cario et al., 2019).

6. Discussion and Conclusions

For terrestrial seawater with salinity exceeding $22\,\mathrm{g\,kg^{-1}}$, water heated by hydrothermal vents becomes buoyant and rises. However, as argued recently by Kang et al. (2022), Enceladus may have an ocean which is considerably

fresher than that on earth, consistent with the chemical equilibrium state obtained from consideration of the Enceladus water-rock ratio in laboratory experiments (Glein et al., 2018; Zolotov, 2007; Zolotov & Postberg, 2014). As shown in Figures 1a, 1c and 1e, the value of α can then be negative for a wide range of depths if the temperature is between -2 to 2°C. If this is so, gravity currents spreading along the sea floor of Enceladus might be the relevant paradigm, rather than plumy convection reaching all the way to the upper boundary. Beyond Enceladus, icy moons with small gravity and oceans which are shallow and fresh, might also be in a regime of negative or very small α. It should be noted that this might only be a transient phase in the evolution of an icy ocean world and the final equilibrium stage might resemble the one proposed in Melosh et al. (2004) and Zeng and Jansen (2021), that is, plumy convection in a bottom layer capped by a stably stratified layer at the top. We have shown here that even at this equilibrium, the convection in the bottom layer will be extremely weak because the fluid is not very buoyant.

In contrast, Europa's ocean is expected to be more saline or have dissolved components which increase the thermal expansion coefficient of seawater. Additionally, its gravity is stronger and associated buoyancy fluxes therefore larger, suggesting that rising plumes might be triggered by hydrothermal activity. Even if Europa's ocean turns out to be fresh, its great depth and larger gravity implies that pressure effects would be a prominent factor in setting the thermodynamic EOS. Figure 1a shows that negative values of α can only be achieved at extremely low salinities ($<5\text{g kg}^{-1}$) and shallow depths (~5 km). Thus, even in this fresh limit, its α would likely be positive supporting plumes of buoyant fluid that ultimately rise to the surface as postulated in Fernando et al. (1998) and Goodman and Lenferink (2012).

In the case that $\alpha > 0$, we contrasted the behavior of plumy convection for which $Ro* \ll 1$ and $Ro* \leq 1$. In the former (typical of Enceladus), plumes become baroclinically unstable before reaching the upper boundary and transit timescales from bottom to top are long, increasing as $Ro*$ becomes smaller. In the latter (more typical of Europa), baroclinic instability occurs after the plumes strike the upper boundary and transit times are much shorter.

In summary, our study explores a fundamental distinction in hydrothermal plume behavior which is sensitive to size and salinity and of which Enceladus and Europa might be representative end-members. Our results could potentially influence which icy moon we decide to visit, at least in the short term. Large moons have stronger gravity, more pressurized oceans, and are more likely to have $\alpha > 0$ enabling buoyant convection in their oceans, irrespective of their salinities. If a large moon like Europa is energized by hydrothermal activity from below, it is likely to have more vigorous convection and more efficient seafloor to ice-shell transport—thus leaving its imprint on the ice shell—than, for example, a small moon such as Enceladus. For missions to smaller moons there are multiple possibilities which are sensitive to the assumed salinity. If their oceans were to be fresh, we would have to estimate the depth of the bottom weakly convective layer and whether imprints from it could reach the ice shell. Thus, if the primary icy-ocean world habitable interface is the seafloor, it may be a more appealing prospect to focus on Europa than Enceladus because our current technological limitations make ice shells much more accessible than the deep ocean. On the other hand, Enceladus's deep ocean could be stratified potentially providing chemical gradients for chemosynthetic life to thrive within the ocean and not just at the seafloor.

Finally, it should be noted that our study has made a number of key simplifications. In particular, our simulations are initialized from a state of rest and the background temperature of the entire water column is assumed to be at the freezing temperature of water just under the ice sheet. If large-scale ocean dynamics are considered, as well as the long-term influence of hydrothermal plumes, the ambient water into which the hydrothermal plumes inject their properties may be very different from that assumed in our study. Thus the influence of the assumed initial state should be explored further.

Additionally, our domain size is small and chosen to study the effect of a single venting system in isolation. However, as baroclinic instability broadens, the convective activity begins to self-interact across the periodic domain. Eventually, the simulation effectively becomes one dimensional as warm water supplied from below can only rise upwards. Given more computational resources to enable us to study larger domains, we would expect plumes to spread horizontally under the action of baroclinic instability and thus the role of lateral eddy-mixing processes to be even more pronounced. Choblet et al. (2017) postulated heating patches of O(50 km) in lateral scale but with lower peak heat fluxes than assumed here. In such a case of weaker fluxes spread over a larger area, we still expect the role of baroclinic instability to be very important and horizontal spreading to be prevalent. Findings from Legg and Marshall (1993) indicate that the heating patch would first be filled with individual

deformation scale plumes held together by a rim current. Eventually, baroclinic instability would develop along this rim and the convective products would break apart and move away from the heating patch. At equilibrium, there would be a balance between the buoyancy supplied from the bottom and the buoyancy leaving the heating patch through lateral translation of plumes breaking off. The height to which, and on what timescale, plumes reach in such a scenario should be a subject of future study.

Data Availability Statement

Oceananigans.jl (Ramadhan et al., 2020, 2023) was used to perform numerical simulations used in this study. Data from the numerical simulations and analysis code used in this study is available at Bire (2023).

References

Ashkenazy, Y., & Tziperman, E. (2021). Dynamic Europa Ocean shows transient Taylor columns and convection driven by ice melting and salinity. *Nature Communications*, *12*(1), 6376. https://doi.org/10.1038/s41467-021-26710-0

Běhounková, M., Tobie, G., Choblet, G., Kervazo, M., Melwani Daswani, M., Dumoulin, C., & Vance, S. D. (2021). Tidally induced magmatic pulses on the oceanic floor of Jupiter's moon Europa. *Geophysical Research Letters*, *48*(3), e2020GL090077. https://doi.org/10.1029/2020gl090077

Beuthe, M., Rivoldini, A., & Trinh, A. (2016). Enceladus's and Dione's floating ice shells supported by minimum stress isostasy. *Geophysical Research Letters*, *43*(19), 10088–10096. https://doi.org/10.1002/2016gl070650

Bire, S. (2023). *Juicymoons plumes*. Zenodo. https://doi.org/10.5281/ZENODO.7502389

Bire, S., Kang, W., Ramadhan, A., Campin, J., & Marshall, J. (2022). Exploring ocean circulation on icy moons heated from below. *Journal of Geophysical Research: Planets*, *127*(3), e2021JE007025. https://doi.org/10.1029/2021je007025

Cable, M. L., Porco, C., Glein, C. R., German, C. R., MacKenzie, S. M., Neveu, M., et al. (2021). The science case for a return to Enceladus. *The Planetary Science Journal*, *2*(4), 132. https://doi.org/10.3847/psj/abfb7a

Čadek, O., Souček, O., & Běhounková, M. (2019). Is Airy isostasy applicable to icy moons? *Geophysical Research Letters*, *46*(24), 14299–14306. https://doi.org/10.1029/2019gl085903

Čadek, O., Tobie, G., Van Hoolst, T., Massé, M., Choblet, G., Lefèvre, A., et al. (2016). Enceladus's internal ocean and ice shell constrained from Cassini gravity, shape, and libration data. *Geophysical Research Letters*, *43*(11), 5653–5660. https://doi.org/10.1002/2016gl068634

Cario, A., Oliver, G. C., & Rogers, K. L. (2019). Exploring the deep marine biosphere: Challenges, innovations, and opportunities. *Frontiers in Earth Science*, *7*. https://doi.org/10.3389/feart.2019.00225

Choblet, G., Tobie, G., Buch, A., Čadek, O., Barge, L. M., Běhounková, M., et al. (2021). *Enceladus as a potential oasis for life: Science goals and investigations for future explorations*. Experimental Astronomy. https://doi.org/10.1007/s10686-021-09808-7

Choblet, G., Tobie, G., Sotin, C., Běhounková, M., Čadek, O., Postberg, F., & Souček, O. (2017). Powering prolonged hydrothermal activity inside Enceladus. *Nature Astronomy*, *1*(12), 841–847. https://doi.org/10.1038/s41550-017-0289-8

Dai, A., & Wu, C.-S. (2016). High-resolution simulations of cylindrical gravity currents in a rotating system. *Journal of Fluid Mechanics*, *806*, 71–101. https://doi.org/10.1017/jfm.2016.598

Dai, A., & Wu, C.-S. (2018). High-resolution simulations of unstable cylindrical gravity currents undergoing wandering and splitting motions in a rotating system. *Physics of Fluids*, *30*(2), 026601. https://doi.org/10.1063/1.5011070

Ede, A. J. (1956). The influence of anomalous expansion on natural convection in water. *Applied Scientific Research*, *5*(6), 458–460. https://doi.org/10.1007/bf03184607

Fernando, H. J. S. (1991). Turbulent mixing in stratified fluids. *Annual Review of Fluid Mechanics*, *23*(1), 455–493. https://doi.org/10.1146/annurev.fl.23.010191.002323

Fernando, H. J. S., Chen, R.-r., & Ayotte, B. A. (1998). Development of a point plume in the presence of background rotation. *Physics of Fluids*, *10*(9), 2369–2383. https://doi.org/10.1063/1.869754

Fifer, L. M., Catling, D. C., & Toner, J. D. (2022). Chemical fractionation modeling of plumes indicates a gas-rich, moderately alkaline Enceladus ocean. *The Planetary Science Journal*, *3*(8), 191. https://doi.org/10.3847/psj/ac7a9f

Fox-Powell, M. G., & Cousins, C. R. (2021). Partitioning of crystalline and amorphous phases during freezing of simulated Enceladus ocean fluids. *Journal of Geophysical Research: Planets*, *126*(1), e2020JE006628. https://doi.org/10.1029/2020je006628

Glass, J., Dierssen, H., Glein, C., Schmidt, B., & Winebrenner, D. (2022). Defining and characterizing habitable environments in ocean world systems. *Oceanography*. https://doi.org/10.5670/oceanog.2021.414

Glein, C., Postberg, F., & Vance, S. D. (2018). *The geochemistry of Enceladus: Composition and controls. In (chap. 3)*. The University of Arizona Press. https://doi.org/10.2458/azu_uapress_9780816537075-ch003

Goodman, J. C., Collins, G. C., Marshall, J., & Pierrehumbert, R. T. (2004). Hydrothermal plume dynamics on Europa: Implications for chaos formation. *Journal of Geophysical Research*, *109*(E3). https://doi.org/10.1029/2003je002073

Goodman, J. C., & Lenferink, E. (2012). Numerical simulations of marine hydrothermal plumes for Europa and other icy worlds. *Icarus*, *221*(2), 970–983. https://doi.org/10.1016/j.icarus.2012.08.027

Griffiths, R. W., & Linden, P. F. (1981). The stability of vortices in a rotating, stratified fluid. *Journal of Fluid Mechanics*, *105*(-1), 283. https://doi.org/10.1017/s0022112081003212

Hand, K., & Chyba, C. (2007). Empirical constraints on the salinity of the Europan Ocean and implications for a thin ice shell. *Icarus*, *189*(2), 424–438. https://doi.org/10.1016/j.icarus.2007.02.002

Hand, K., Sotin, C., Hayes, A., & Coustenis, A. (2020). On the habitability and future exploration of ocean worlds. *Space Science Reviews*, *216*(5), 95. https://doi.org/10.1007/s11214-020-00713-7

Hansen, C. J., Esposito, L., Stewart, A. I. F., Colwell, J., Hendrix, A., Pryor, W., et al. (2006). Enceladus' water vapor plume. *Science*, *311*(5766), 1422–1425. https://doi.org/10.1126/science.1121254

Helfrich, K. R. (1994). Thermals with background rotation and stratification. *Journal of Fluid Mechanics*, *259*, 265–280. https://doi.org/10.1017/s0022112094000121

Hemingway, D. J., & Mittal, T. (2019). Enceladus's ice shell structure as a window on internal heat production. *Icarus*, *332*, 111–131. https://doi.org/10.1016/j.icarus.2019.03.011

Hsu, H.-W., Postberg, F., Sekine, Y., Shibuya, T., Kempf, S., Horányi, M., et al. (2015). Ongoing hydrothermal activities within Enceladus. *Nature*, *519*(7542), 207–210. https://doi.org/10.1038/nature14262

Ingersoll, A. P., & Nakajima, M. (2016). Controlled boiling on Enceladus. 2. Model of the liquid-filled cracks. *Icarus*, *272*, 319–326. https://doi.org/10.1016/j.icarus.2015.12.040

Ivanov, D., & Nikolov, S. (2020). The anomalous thermal expansion of water. *Physics Education*, *55*(5), 055008. https://doi.org/10.1088/1361-6552/ab9480

Jones, H., & Marshall, J. (1993). Convection with rotation in a neutral ocean: A study of open-ocean deep convection. *Journal of Physical Oceanography*, *23*(6), 1009–1039. https://doi.org/10.1175/1520-0485(1993)023⟨1009:cwrian⟩2.0.co;2

Kang, W., Mittal, T., Bire, S., Campin, J.-M., & Marshall, J. (2022). How does salinity shape ocean circulation and ice geometry on Enceladus and other icy satellites? *Science Advances*, *8*(29). https://doi.org/10.1126/sciadv.abm4665

Khawaja, N., Postberg, F., Hillier, J., Klenner, F., Kempf, S., Nölle, L., et al. (2019). Low-mass nitrogen-oxygen-bearing, and aromatic compounds in Enceladean ice grains. *Monthly Notices of the Royal Astronomical Society*, *489*(4), 5231–5243. https://doi.org/10.1093/mnras/stz2280

Kvorka, J., Čadek, O., Tobie, G., & Choblet, G. (2018). Does Titan's long-wavelength topography contain information about subsurface ocean dynamics? *Icarus*, *310*, 149–164. https://doi.org/10.1016/j.icarus.2017.12.010

Legg, S., & Marshall, J. (1993). A heton model of the spreading phase of open-ocean deep convection. *Journal of Physical Oceanography*, *23*(6), 1040–1056. https://doi.org/10.1175/1520-0485(1993)023⟨1040:ahmots⟩2.0.co;2

MacKenzie, S. M., Neveu, M., Davila, A. F., Lunine, J. I., Cable, M. L., Phillips-Lander, C. M., et al. (2022). Science objectives for flagship-class mission concepts for the search for evidence of life at Enceladus. *Astrobiology*, *22*(6), 685–712. https://doi.org/10.1089/ast.2020.2425

Marshall, J., Adcroft, A., Hill, C., Perelman, L., & Heisey, C. (1997). A finite-volume, incompressible Navier Stokes model for studies of the ocean on parallel computers. *Journal of Geophysical Research*, *102*(C3), 5753–5766. https://doi.org/10.1029/96jc02775

Maxworthy, T., & Narimousa, S. (1994). Unsteady, turbulent convection into a homogeneous, rotating fluid,with oceanographic applications. *Journal of Physical Oceanography*, *24*(5), 865–887. https://doi.org/10.1175/1520-0485(1994)024⟨0865:utciah⟩2.0.co;2

Melosh, H., Ekholm, A., Showman, A., & Lorenz, R. (2004). The temperature of europa's subsurface water ocean. *Icarus*, *168*(2), 498–502. https://doi.org/10.1016/j.icarus.2003.11.026

Millero, F. J., Feistel, R., Wright, D. G., & McDougall, T. J. (2008). The composition of standard seawater and the definition of the reference-composition salinity scale. *Deep Sea Research Part I: Oceanographic Research Papers*, *55*(1), 50–72. https://doi.org/10.1016/j.dsr.2007.10.001

Nimmo, F., & Pappalardo, R. T. (2016). Ocean worlds in the outer solar system. *Journal of Geophysical Research: Planets*, *121*(8), 1378–1399. https://doi.org/10.1002/2016je005081

Porco, C. C., Helfenstein, P., Thomas, P. C., Ingersoll, A. P., Wisdom, J., West, R., et al. (2006). Cassini observes the active south pole of Enceladus. *Science*, *311*(5766), 1393–1401. https://doi.org/10.1126/science.1123013

Postberg, F., Kempf, S., Schmidt, J., Brilliantov, N., Beinsen, A., Abel, B., et al. (2009). Sodium salts in e-ring ice grains from an ocean below the surface of Enceladus. *Nature*, *459*(7250), 1098–1101. https://doi.org/10.1038/nature08046

Postberg, F., Khawaja, N., Abel, B., Choblet, G., Glein, C. R., Gudipati, M. S., et al. (2018). Macromolecular organic compounds from the depths of Enceladus. *Nature*, *558*(7711), 564–568. https://doi.org/10.1038/s41586-018-0246-4

Postberg, F., Klenner, F., Zou, Z., Hillier, J. K., Khawaja, N., Nölle, L., & Schmidt, J. (2022). Detection of phosphates originating from Enceladus' ocean by Cassini's cosmic dust analyzer. In *Europlanet science congress 2022, Granada, Spain, 18–23 September 2022, EPSC2022-639*. https://doi.org/10.5194/epsc2022-639

Ramadhan, A., Wagner, G., Hill, C., Campin, J.-M., Churavy, V., Besard, T., et al. (2020). Oceananigans.jl: Fast and friendly geophysical fluid dynamics on GPUs. *Journal of Open Source Software*, *5*(53). https://doi.org/10.21105/joss.02018

Ramadhan, A., Wagner, G. L., Constantinou, N. C., Silvestri, S., Chor, T., Poulin, F. J., et al. (2023). *Clima/oceananigans.jl: v0.87.1*. Zenodo. https://doi.org/10.5281/ZENODO.8280097

Roquet, F., Madec, G., Brodeau, L., & Nycander, J. (2015). Defining a simplified yet "realistic" equation of state for seawater. *Journal of Physical Oceanography*, *45*(10), 2564–2579. https://doi.org/10.1175/jpo-d-15-0080.1

Rovira-Navarro, M., Katz, R. F., Liao, Y., van der Wal, W., & Nimmo, F. (2022). The tides of Enceladus' porous core. *Journal of Geophysical Research: Planets*, *127*(5), e2021JE007117. https://doi.org/10.1029/2021je007117

Saunders, P. M. (1973). The instability of a baroclinic vortex. *Journal of Physical Oceanography*, *3*(1), 61–65. https://doi.org/10.1175/1520-0485(1973)003⟨0061:tioabv⟩2.0.co;2

Sekine, Y., Shibuya, T., Postberg, F., Hsu, H.-W., Suzuki, K., Masaki, Y., et al. (2015). High-temperature water–rock interactions and hydrothermal environments in the chondrite-like core of Enceladus. *Nature Communications*, *6*(1), 8604. https://doi.org/10.1038/ncomms9604

Soderlund, K. M. (2019). Ocean dynamics of outer solar system satellites. *Geophysical Research Letters*, *46*(15), 8700–8710. https://doi.org/10.1029/2018gl081880

Soderlund, K. M., Schmidt, B. E., Wicht, J., & Blankenship, D. D. (2013). Ocean-driven heating of Europa's icy shell at low latitudes. *Nature Geoscience*, *7*(1), 16–19. https://doi.org/10.1038/ngeo2021

Speer, K. G., & Marshall, J. (1995). The growth of convective plumes at seafloor hot springs. *Journal of Marine Research*, *53*(6), 1025–1057. https://doi.org/10.1357/0022240953212972

Steel, E. L., Davila, A., & McKay, C. P. (2017). Abiotic and biotic formation of amino acids in the Enceladus Ocean. *Astrobiology*, *17*(9), 862–875. https://doi.org/10.1089/ast.2017.1673

Tebo, B. M., Nealson, K. H., Emerson, S., & Jacobs, L. (1984). Microbial mediation of Mn(II) and Co(II) precipitation at the O_2/H_2S interfaces in two anoxic fjords. *Limnology & Oceanography*, *29*(6), 1247–1258. https://doi.org/10.4319/lo.1984.29.6.1247

Thomas, P., Tajeddine, R., Tiscareno, M., Burns, J., Joseph, J., Loredo, T., et al. (2016). Enceladus's measured physical libration requires a global subsurface ocean. *Icarus*, *264*, 37–47. https://doi.org/10.1016/j.icarus.2015.08.037

Travis, B., Palguta, J., & Schubert, G. (2012). A whole-moon thermal history model of Europa: Impact of hydrothermal circulation and salt transport. *Icarus*, *218*(2), 1006–1019. https://doi.org/10.1016/j.icarus.2012.02.008

Trumbo, S. K., Brown, M. E., & Hand, K. P. (2019). Sodium chloride on the surface of Europa. *Science Advances*, *5*(6), eaaw7123. https://doi.org/10.1126/sciadv.aaw7123

Vance, S., Bouffard, M., Choukroun, M., & Sotin, C. (2014). Ganymedes internal structure including thermodynamics of magnesium sulfate oceans in contact with ice. *Planetary and Space Science*, *96*, 62–70. https://doi.org/10.1016/j.pss.2014.03.011

Vance, S., Panning, M. P., Stähler, S., Cammarano, F., Bills, B. G., Tobie, G., et al. (2018). Geophysical investigations of habitability in ice-covered ocean worlds. *Journal of Geophysical Research: Planets*, *123*(1), 180–205. https://doi.org/10.1002/2017je005341

Van Hoolst, T., Baland, R.-M., & Trinh, A. (2016). The diurnal libration and interior structure of Enceladus. *Icarus*, *277*, 311–318. https://doi.org/10.1016/j.icarus.2016.05.025

Waite, J. H., Glein, C. R., Perryman, R. S., Teolis, B. D., Magee, B. A., Miller, G., et al. (2017). Cassini finds molecular hydrogen in the Enceladus plume: Evidence for hydrothermal processes. *Science*, *356*(6334), 155–159. https://doi.org/10.1126/science.aai8703

Zeng, Y., & Jansen, M. F. (2021). Ocean circulation on Enceladus with a high-versus low-salinity Ocean. *The Planetary Science Journal*, *2*(4), 151. https://doi.org/10.3847/psj/ac1114

Zolotov, M. Y. (2007). An oceanic composition on early and today's Enceladus. *Geophysical Research Letters*, *34*(23), L23203. https://doi.org/10.1029/2007gl031234

Zolotov, M. Y., & Postberg, F. (2014). Can nano-phase silica originate from chondritic fluids? The application to Enceladus' SiO_2 particles. *Lunar and Planetary Science Conference Abstracts*, (1777), 2496.